Characterization of rust on ancient Indian iron

R. Balasubramaniam[†,*], A. V. Ramesh Kumar[#] and P. Dillmann[‡]

[†]Department of Materials and Metallurgical Engineering, Indian Institute of Technology, Kanpur 208 016, India
[#]Electrochemistry and Corrosion Division, Defence Materials and Stores Research and Development Establishment, Kanpur 208 013, India
[‡]Laboratoire Pierre Süe CEA/CNRS, CE Saclay 91191 Gif sur Yvette Cedex, France and IRAMAT UMR5060 CNRS, France

Experimental techniques for qualitative and quantitative analysis of rust have been reviewed. Rusting of iron in atmospheric and soil environments has also been briefly reviewed. The application of important spectroscopic methods (like Raman spectroscopy, infrared spectroscopy and Mössbauer spectroscopy) has been highlighted. X-ray diffraction techniques to understand global as well as local character of rust have been discussed. The techniques have been illustrated with suitable examples of atmospheric rust on ancient Indian irons.

THE exalted position of ancient Indian iron metallurgy has been well-discussed in the literature[1–12]. Recent scientific studies have highlighted several unknown technical aspects of ancient Indian metallurgical skill[11–15]. While iron made its appearance in the Indian subcontinent around 1500 BC, its widespread use was established by the 8th Century BC. The excellent atmospheric corrosion resistance exhibited by several world-famous Indian irons, for example, the Delhi[11] and Dhar[12] iron pillars, the Konarak iron beams[16,17], etc., has been well documented. The study of ancient iron and its corrosion, therefore, is important in the Indian context. There are a variety of techniques to understand the basic electrochemical nature and aqueous corrosion tendency of metallic alloys[18,19]. Readers interested in understanding techniques to evaluate corrosion behaviour can consult standard references[20,21]. The focus of the present review is on rust characterization, specifically addressing atmospheric rust on ancient Indian irons. All the techniques, except perhaps Mössbauer spectroscopy, can be applied for characterizing corrosion products on other metallic materials.

Several different techniques can be used in different stages of investigation. The basic techniques involved are essentially material characterization techniques for surface analyses[22]. Microscopy-related techniques are useful in understanding the topological state of the corroded layers and in analysing their cross-sections. Composition analysis techniques provide valuable information about variations across rusts. Several different methods are available for identifying corrosion products on iron[22]. The review will first introduce rust. Rusting in atmospheric and soil environments will be briefly reviewed. Techniques for microstructural, compositional and phase analyses will follow sequentially.

*For correspondence. (e-mail: bala@iitk.ac.in)

Rust

Rust is a reddish-brown corrosion product of iron consisting of several different constituents[23,24]. Hydrous ferrous oxide ($FeO.nH_2O$) or ferrous hydroxide ($Fe(OH)_2$) is the first diffusion-barrier layer formed on the surface. As the pH of saturated $Fe(OH)_2$ is about 9.5, the surface of iron corroding in aerated pure water is always alkaline. The colour of $Fe(OH)_2$ is normally green to greenish-black because of incipient oxidation by air and these intermediates have been frequently referred to as green complexes or green rust. At the outer surface of the layer, access to dissolved oxygen converts ferrous oxide to hydrous ferric oxide or ferric hydroxide according to the following reaction.

$$Fe(OH)_2 + \tfrac{1}{2} O_2 \rightarrow Fe(OH)_3. \quad (1)$$

Hydrous ferric oxide is orange to red-brown in colour and comprises most of ordinary rust. It exists as non-magnetic α-Fe_2O_3 (hematite) or magnetic γ-Fe_2O_3 (maghemite). The α-form possesses greater negative free energy of formation (i.e. greater stability). Saturated $Fe(OH)_3$ is nearly neutral in pH. A magnetic hydrous ferrous ferrite, $Fe_3O_4.nH_2O$, often forms a black intermediate layer between hydrous Fe_2O_3 and FeO. Ideally, rust films consist of three layers of iron oxide in different states of oxidation. Rust layers are not protective because they are permeable to air and water. Therefore, iron continues to corrode even after rust has formed.

Atmospheric environment is important to corrosion scientists, archaeologists and conservators. The corrosion or rusting of iron in the atmosphere occurs by the well-known reaction

$$2Fe + H_2O + \tfrac{1}{2} O_2 \rightarrow 2FeOOH. \quad (2)$$

Metal dissolution is the anodic partial reaction, while the dominant cathodic reaction is oxygen reduction. Although hydrogen reduction may also support the anodic reaction, its rate is much lower because the electrolyte on the surface of iron-based materials is well buffered, ranging in pH between 5.8 and 7. Wetting-and-drying cycles are

involved in atmospheric corrosion. The presence of a thick electrolyte layer on the surface can limit oxygen reduction rate. In such situations, the following reduction reaction supports oxidation of iron

$$8FeOOH + Fe^{2+} + 2e \rightarrow 3Fe_3O_4 + 4H_2O. \quad (3)$$

The subsequent reactions by which macroscopically thick rust scales develop on pure iron have been analysed[25–27]. The oxidation of the Fe^{2+} ions in green complexes and green rust, leads to formation of lepidocrocite (*g*-FeOOH) in well-aerated systems and magnetite in oxygen-depleted systems. The rust composition, therefore, changes with time (and metal composition). On pure iron, *g*-FeOOH transforms to the more stable goethite (*a*-FeOOH) and some spinel. With increasing time, goethite converts to either maghemite or hematite. Conversion to hematite usually requires higher temperatures. Although the formation of several other phases (like amorphous phases, ferrihydride $Fe(OH)_2$, *d*-FeOOH, etc.) have been reported, there is no general agreement on their specific role in atmospheric corrosion.

Different views exist on the multi-layered rust scales on weathering steels. For example, the inner adherent layer has been shown to be comprised of *a*-FeOOH and *g*-FeOOH, while the outer layers were composed of amorphous hydroxides and *d*-FeOOH[28]. The rust on weathering steel after 16 years of exposure in a rural environment was composed of two layers, with the inner dull layer comprising nanosized particles of *a*-FeOOH and the outer bright layer, *g*-FeOOH[29]. The rust on weathering steel after 25 years of exposure in an industrial environment exhibited similar characteristics, i.e. an inner layer consisting of nanosized goethite and an external layer of lepidocrocite[30].

Different forms of iron corrosion products along with their lattice parameters are provided in Table 1. Formation of nitrate- or carbonate-containing corrosion products is sparse. Atmospheric corrosion of iron is accelerated by the presence of chlorides, which may result in the formation of basic iron (II, III) chlorides and akaganeite (*b*-FeOOH).

Table 1. Lattice parameters (*a*, *b* and *c*) of metallic iron and its main corrosion products

Substance	*a*	*b*	*c*	Density (g/cc)	Structure
a-Fe	2.866			7.86	bcc
b-Fe	3.647				fcc
FeO (wüstite)	4.30			5.67	fcc
a-FeOOH (goethite)	4.60	10.01	3.04	4.28	Orthorhombic
b-FeOOH (akaganeite)	10.52		3.028	3.55	Tetragonal
g-FeOOH (lepidocrocite)	3.65	12.50	3.07	4.09	Orthorhombic
d-FeOOH	2.94	4.49	3.8		Hexagonal
FeOOH (Gel)	8.37				Cubic
a-Fe_2O_3 (hematite)	5.035	13.72	5.26		Trigonal
g-Fe_2O_3 (maghemite)	8.33		24.99	4.69	Cubic
Fe_3O_4 (magnetite)	8.396			5.175	Cubic
$Fe(OH)_2$	3.27		4.62	3.40	Trigonal
$FeCO_3$ (siderite)	4.711		15.436	3.83	Trigonal

As regards the morphology of atmospheric rust scales, the outer part of the scale is normally cracked, with extremely small (4–15 nm) pore sizes[31] and large surface (50 m^2/g) areas[24]. The atmospheric corrosion rates for iron are relatively high and exceed that of structural steel. They range (in μm/year) between 4 and 65 for rural, 26 and 104 for marine, 23 and 71 for urban, and between 26 and 175 for industrial environments[32].

In addition to the atmospheric environment, another important environment in which archaeological iron can undergo corrosion is soil. The corrosion aspects of iron and steel approximate to that in total immersion in water[18,19]. The rates of soil corrosion of iron, however, resemble that observed in atmospheric exposure. The rates are controlled primarily by the diffusion of oxygen in water entrapped in the soil. The important factors that affect soil corrosion are soil composition, porosity (i.e. aeration), electrical conductivity, dissolved salts, moisture content and acidity/alkalinity. Soil corrosivity is not directly related to any of these features; the relationships are rather complicated[33].

Microstructural analysis

The scanning electron microscope (SEM) is the first analytical instrument used for quick observations[34]. The optical microscope can be used for imaging the surface but it has limitations of resolution and depth of field at higher magnifications. The SEM can be used for high-resolution imaging of the surface, with a large depth of field. The degree of corrosion, surface morphology, particle size and texture can be effectively studied in the SEM. Recent developments include atomic force microscopy, where atomic-level resolutions are possible[34]. Interestingly, neither the atomic force microscope nor the transmission electron microscope has been utilized to study rusts on ancient Indian iron. These are possible subjects for future detailed studies.

As an example, the nature of growing rust on the surface of Dhar pillar iron will be addressed[35,36]. The fracture surface of a sample from the Dhar pillar iron was observed after a period of 12 months. The rust was heterogeneous in nature (Figure 1 *a*)[35]. At some locations the external scale was cracked, while at other locations, globular protrusions were observed on the surface. These nodular structures, at higher magnifications, were composed of flowery needle-like rust (Figure 1 *b*)[35] growing on top of a cracked rust layer. The growth of the flowery needle-like rust was evident in areas where considerable cracking was observed in the outer layer, indicating that this rust grew at locations where the outer oxide rust layer was cracked[30,31]. Cross sectional microscopy of the transversely mounted Dhar pillar iron sample provided macroscopic details of the rust structure (Figure 1 *c*)[35]. The layered nature of rust is a typical observation. The optical microscope can also be used for studying rust cross-sections at lower magnifications.

Compositional analysis

X-rays that are emitted from the interaction volume of the electron beam with the surface can be utilized for both qualitative and quantitative compositional analysis, by techniques of EDS (energy dispersive spectroscopy) or WDS (wavelength dispersive spectroscopy)[34]. These spectroscopy units are generally available in SEMs. In cases when rigorous compositional analyses are required, the electron probe microanalyser (EPMA) is the equipment of choice. The compositions determined in the EPMA are more precise due to the standardization procedure. The analysis procedure is time-consuming because standard spectra are obtained for each analysis from the standard reference samples that are preloaded in the sample-holding unit of the EPMA[34].

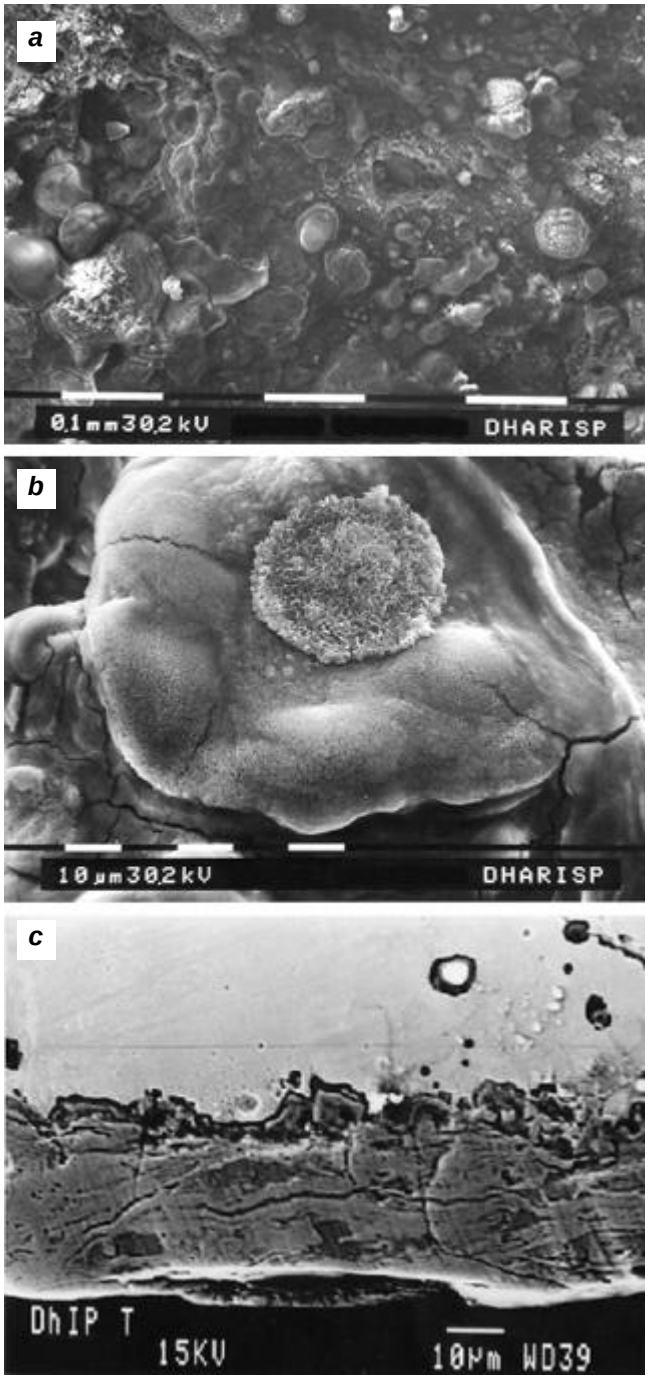

Figure 1. Dhar iron pillar: ***a***, Nature of the growing rust on the fracture surface of the Dhar pillar iron. Notice the heterogeneous nature of rust. ***b***, Several of the nodular features noticed in ***a*** were composed of flowery needle-like rust. ***c***, Cross-section of the atmospheric rust observed in the SEM (ref. 35).

The important role of phosphorus in imparting superior corrosion resistance in ancient Indian irons has now been recognized[11,35]. Phosphorus can be present either in the non-metallic slag inclusions as a compound or in ferrite as a solid solution. It is necessary to obtain elemental concentration profiles near locations of interest; for example, the slag/matrix interface or oxide/matrix interface, because phosphorus is distributed non-homogeneously in the matrix due to micro-segregation.

The compositional variations were determined using an EPMA in a Gupta period Deogarh iron as a function of distance in the rust. The rust was essentially composed of iron oxides and oxyhydroxides. The precise nature of the iron oxyhydroxide/oxide could not be determined by the EPMA analysis. The inner region possessed a relatively high and uniform P content, which decreased on moving towards the scale–environment interface. Another powerful technique to detect minor and trace elements is the micro particles-induced X-ray emission (µPIXE) technique[37]. The PIXE method using an EDS detector is a convenient method to chemically analyse the sample because it quantifies relatively low amounts of elements (Z higher than 12) and allows simultaneous multi-elemental analyses. The variation of P content in the matrix and rust of a Gupta-period Eran iron was studied by µPIXE. The 1.5 MeV proton beam of the Pierre Süe Laboratory (at Commissariat à l′Energie Atomique, Saclay, France) nuclear microprobe was used. This energy was selected to favour the X-ray emission corresponding to the lighter elements. The detailed experimental procedure is provided elsewhere[38]. A reference sample of low-alloyed steel containing 450 ppm phosphorus was utilized. Phosphorus-concentration profiles, obtained in the metallic matrix near-slag inclusions, revealed decreasing P content near the slag inclusion (for distances less than 10 µm), which has been related to the dephosphorizing power of the slag[39]. The variation in P content as a function of distance into the atmospheric rust of Eran iron provided important insights (Figure 2)[40]. Significant enrichment of P could be noticed in the oxide scale. At locations where the P content was relatively low in the metallic matrix (square datapoints in Figure 2), there was a higher amount of P, especially at the scale–metal interface, and this continued into the scale. However, with increasing distance into the scale, the P content decreased. The µPIXE study clearly proved the enrichment of P content at the metal–scale interface and in the near vicinity

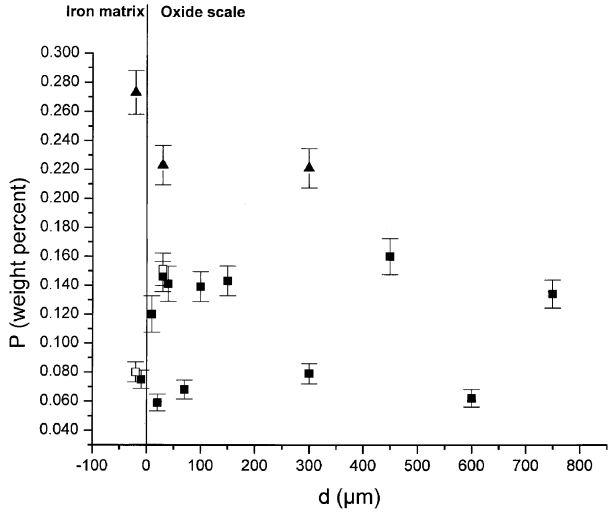

Figure 2. Variation of P content as a function of distance from the metal–oxide interface in Eran iron[40]. Three different profiles obtained at three different locations are provided. The profiles based on datapoints represented by the open and closed squares were obtained at locations where the P content was relatively low in the metallic matrix just below the scale. The profile based on the datapoints represented by triangles was obtained at a location where the P content was relatively high.

of the oxide scale, in regions both rich and poor in phosphorus[40].

Raman spectroscopy

Raman spectroscopy is a powerful tool to study the internal structure of molecules and structures. Raman spectra provide unique information about molecular patterns, spacing, and bonding. Raman spectroscopy is based on the Raman effect, which is the inelastic scattering of photons by molecules, discovered[41] by the Indian physicist C. V. Raman in 1928, for which he received the Nobel Prize in physics in 1930. Basic texts can be referred for further information[42,43]. Corrosion products can be successfully identified using Raman spectroscopy, as every compound possesses a typical Raman spectrum. Small amounts of corrosion products are required and fibre optics can be coupled for remote sensing of data, particularly useful for aqueous systems. Table 2 provides the important bands of some common corrosion products of iron[44]. Minor differences have been noted in the literature due to differences in specimen composition, morphology, sampling and source power. The Raman spectra of various reagent-grade iron oxides and oxyhydroxides are provided in Figure 3 (ref. 44).

An example of application of Raman spectroscopy will be provided below, highlighting the power of conducting experiments with fine beams. Micro-Raman analyses were performed on the polished cross-section of Deogarh iron using a Jobin Yvon-Horiba LabRam Infinity spectrometer and a frequency-doubled Nd: YAG laser at 532 nm

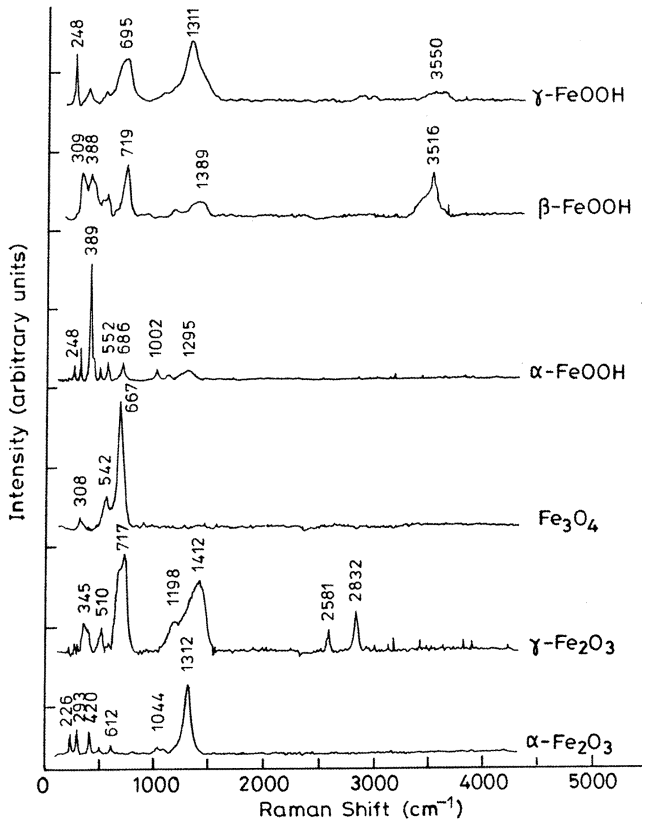

Figure 3. Raman spectra of various reagent-grade iron oxides and iron oxyhydroxides[44].

Table 2. Main Raman bands of reference iron oxide compounds (in cm^{-1}). The strongest peak in each compound has been underlined[44]

Magnetite	Hematite	Maghemite	Goethite	Lepidocrocite
Fe_3O_4	*a*-Fe_2O_3	*g*-Fe_2O_3	*a*-FeOOH	*g*-FeOOH
550	225	193	250	252
670	247	263	300	380
	299	350	385	660
	412	380	470	
	500	505	560	
	613	650–740		

(Dillmann *et al.*, unpublished). Spectral resolution of this set-up is about 2 cm^{-1}. Measurements were made with a × 100 long-focus Leitz objective which provided a beam waist diameter of about 3 μm. Excitation laser power on sample was filtered at least below 0.6 mW in order to avoid thermal effect for the sensitive iron oxides and oxyhydroxides. Two phases were unambiguously detected and identified from literature data and standard material, as goethite (Figure 4 *a*) and magnetite (Figure 4 *b*). However, as the intensity of the magnetite Raman signal is much weaker than that of goethite and because some goethite peaks overlap the magnetite principal band, it is not possible to ensure unambiguously from the spectra that no magnetite is present in goethite. Moreover, a third phase was identified at some locations (Figure 4 *c*) (Dillmann

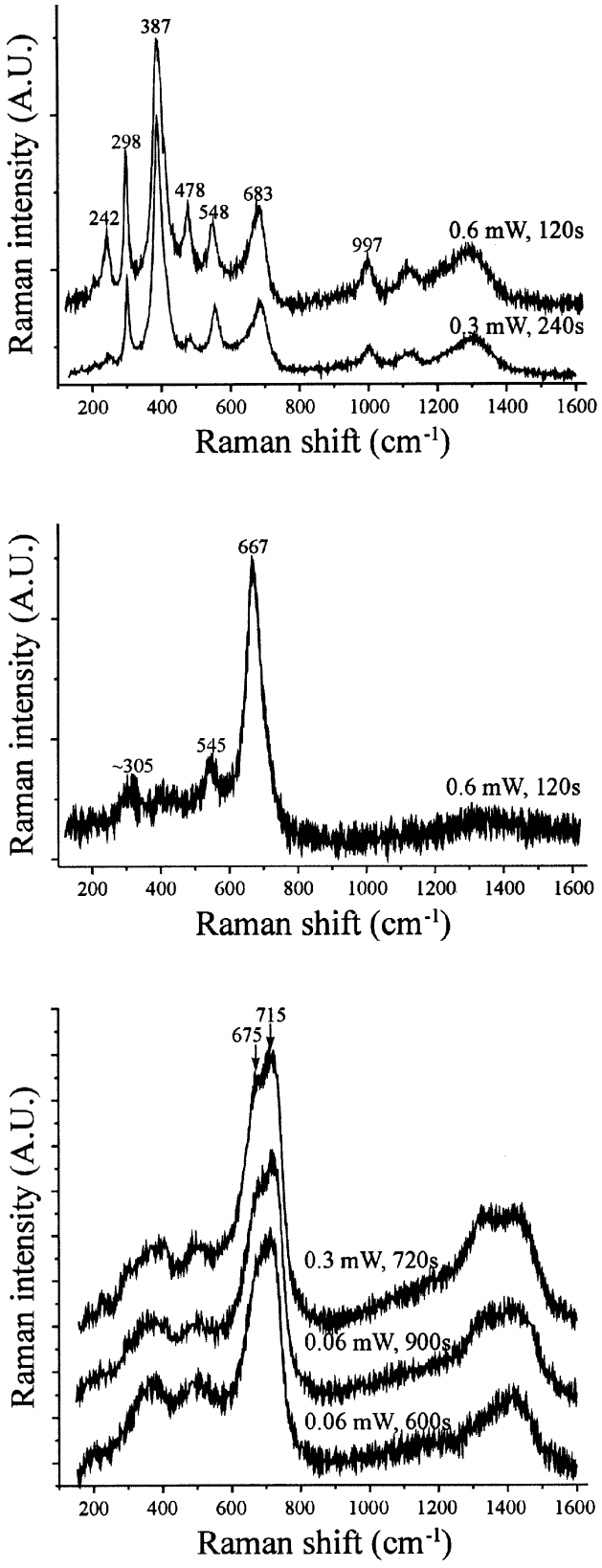

Figure 4. Raman spectra recorded at specific locations in the cross-section of Deogarh iron rust. Laser power and accumulation time are specified for each spectrum. ***a***, Spectra of goethite, two different locations with different laser power. ***b***, Spectrum of magnetite. ***c***, Spectra of maghemite, three different locations with different laser power (Dillmann *et al*., unpublished).

et al., unpublished), which was in relatively good agreement with the maghemite signature. The rust was therefore composed of magnetite, maghemite and goethite. In the light-grey zones on the optical microphotograph presented in Figure 5 (Dillmann *et al*., unpublished), only maghemite and magnetite are present. The dark zones contain goethite and maybe small amounts of magnetite or maghemite. Recent developments include ultrasensitive Raman imaging microscopy, where selected areas can be mapped for the phase distribution using important Raman peak shifts of the phases.

Infrared spectroscopy

The infrared (IR) region of the electromagnetic spectrum extends from a wavelength of about 800 nm towards longer wavelengths. As the characteristic absorption frequencies depend on the molecular environment due to the neighbouring groups, IR spectroscopy can be used to fingerprint these groups and hence deduce the various phases[43]. The spectrum at long wavelengths (1000 to 400 cm^{-1}) provides valuable information regarding the iron–oxygen lattice. Water coordinated as a ligand in the inner sphere of the metal ion as well as wagging, twisting and rocking modes of vibrations are manifested in this region[43]. Oxides generally exhibit fully broadbands due to high degeneracy of the vibration, thermal broadening of the lattice dispersion, and mechanical scattering from powdered sample. In a few cases, M–O stretching vibration can also be present. Corrosion products can be characterized from the known resonant frequencies of various vibrations[45]. The characteristic absorption frequencies of the key bands, which are useful in the identification of phases encountered in iron corrosion products[46–49], are listed in Table 3. The IR spectra can be useful, especially

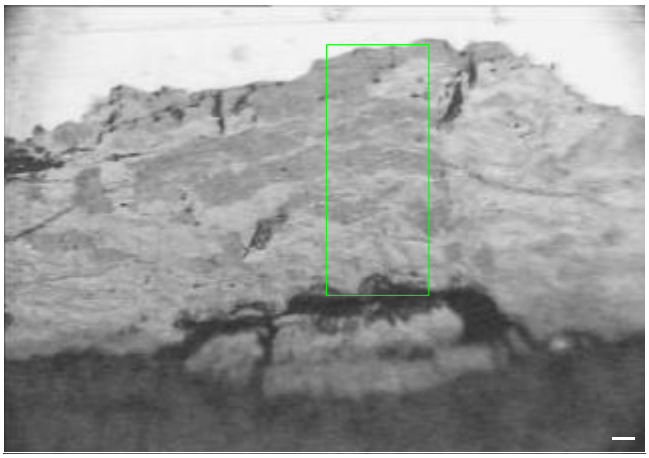

Figure 5. Optical photomicrograph of internal corrosion products in Deogarh iron from where the Raman spectra were recorded (Dillmann *et al*., unpublished). In the light-grey zones, only maghemite and magnetite are present, while the dark zones contain goethite and maybe small amounts of magnetite or maghemite.

in definite identification of certain species such as *a*-FeOOH which is super-paramagnetic at room temperature and therefore indistinguishable from *g*-FeOOH by Mössbauer spectroscopy. Furthermore, at liquid nitrogen temperature, *a*-FeOOH has an internal field similar to that of magnetite and hence its Mössbauer spectrum overlaps that of magnetite. Similarly, ultra-fine particles of *a*-FeOOH are amorphous to X-rays and hence may not show up in XRD patterns, whereas they can be revealed in the IR spectrum.

The IR spectrum of Dhar iron pillar rust is shown in Figure 6 (ref. 49). The presence of *a*-Fe_2O_3 (peak appearing at 572 cm^{-1}), *g*-FeOOH (peak appearing at 1023 cm^{-1} and its shoulder at 791 cm^{-1}), *a*-FeOOH (peak appearing at 884 cm^{-1}) and *d*-FeOOH (peak appearing at 465 cm^{-1}) were confirmed. Ishii and Nakahira[50] confirmed that the Fe–O stretching vibration in iron oxides corresponds to a wavenumber, 570 cm^{-1}. The peak appearing at 572 cm^{-1} is indicative of Fe–O vibration in the oxide of iron. The exact nature of this oxide could not be determined from the IR spectrum, but was revealed by Mössbauer spectroscopy, from which it was concluded that it arises due to Fe–O vibration in *a*-Fe_2O_3[35]. A shoulder in the IR spectrum (Figure 6) corresponding to phosphate ions could be discerned (1030 to 1120 cm^{-1}), indicating that ionic phosphates were present in the rust that was studied.

Mössbauer spectroscopy

Mössbauer spectroscopy or nuclear resonance fluorescence (Mössbauer effect) spectroscopy is defined as recoilless emission of *g*-rays (only low energy) and their resonant absorption by the same kind of atoms. It is also called zero phonon absorption. This effect was discovered by Rudolf Mössbauer[51] in 1958, for which he was awarded the Nobel Prize. While comparing the scattering of 129 KeV gamma rays of Ir^{191} by Ir and Pt, Mössbauer found an increase in the scattering of gamma rays in Ir at low temperature, which was counter to classical predictions. Mössbauer brought in new ideas in the analysis of the emission and scattering of gamma rays by atoms bound in solids. Books dealing with the basic principle and applications of Mössbauer spectroscopy may be referred for further information[52,53]. Three kinds of hyperfine interactions (isomeric shift or chemical shift or centre shift[54], quadrupole splitting[54], and magnetic hyperfine splitting[55]) available in a Mössbauer spectrum are used in rust characterization.

Mössbauer spectroscopy is an important tool for studying Fe (and Sn) corrosion products, because it is a practical method for determining the coordination and oxidation state of Fe. No special sample preparation is needed, which ensures that the exact nature of corrosion products is unambiguously reflected during the investigation. A single spectrum provides three Mössbauer parameters which are distinctly different for the oxides, oxyhydroxides and hydroxides of iron. There is no interference due to presence of species of metals other than iron. The characteristics of passive films can be understood *in situ* using conversion electron Mössbauer spectroscopy. Several specific materials properties can be measured, which include particle size (volume), microscopic magnetic properties (sublattice magnetization opposed to bulk magnetization) and ionic charge. It is also possible to understand the thickness of the growth along with quantitative estimates of individual products. However, these measurements are not easy due to difficulties in spectral analysis and data interpretation, the limited numbers of Mössbauer isotopes, cryogenic requirements and radiation usage. Additionally, sample constraints have also to be understood[52,53].

Several research articles[56–63] and a few review articles[64–67] describe the use of Mössbauer spectroscopy in characterization of iron oxides. Figure 7 (ref. 67) shows the standard Mössbauer spectra of corrosion products commonly found in rust.

A typical Mössbauer spectrum obtained from a Gupta-period Eran iron rust is shown in Figure 8 (ref. 68). The doublet (peak 1) indicated the presence of *g*-FeOOH, *g*-FeOOH and *d*-FeOOH in superparamagnetic form. The

Table 3. Key bands of some common iron corrosion products useful for phase identification by IR spectroscopy (s, Strong; m, Medium; b, Broad)[47–49]

Phase	Absorption frequency (cm^{-1})
a-FeOOH	800(s), 900(s), 610(m)
b-FeOOH	660–710(sb), 850(mb), 3400–3500(sb)
g-FeOOH	755(s), 1020(s), 1170(b)
d-FeOOH	450(sb), 670(m), 920(m), 1130(m), 3320(m)
Fe_3O_4	500–575(b), 380–410(vb)
a-Fe_2O_3	470(s), 540–610(sb), 1105(m)
$Fe(OH)_2$	480, 3630
Green rust	670, 800, 3540
$FePO_4$	575(b), 665(s), 690(s), 1035(m), 1069(s)

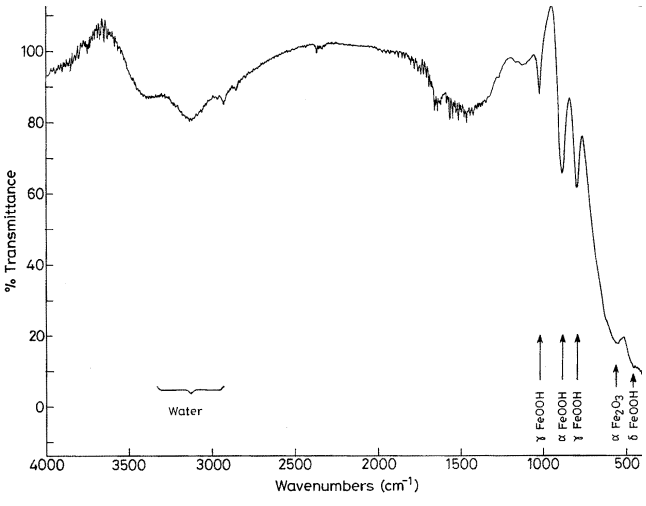

Figure 6. IR spectrum from Dhar iron pillar rust[49].

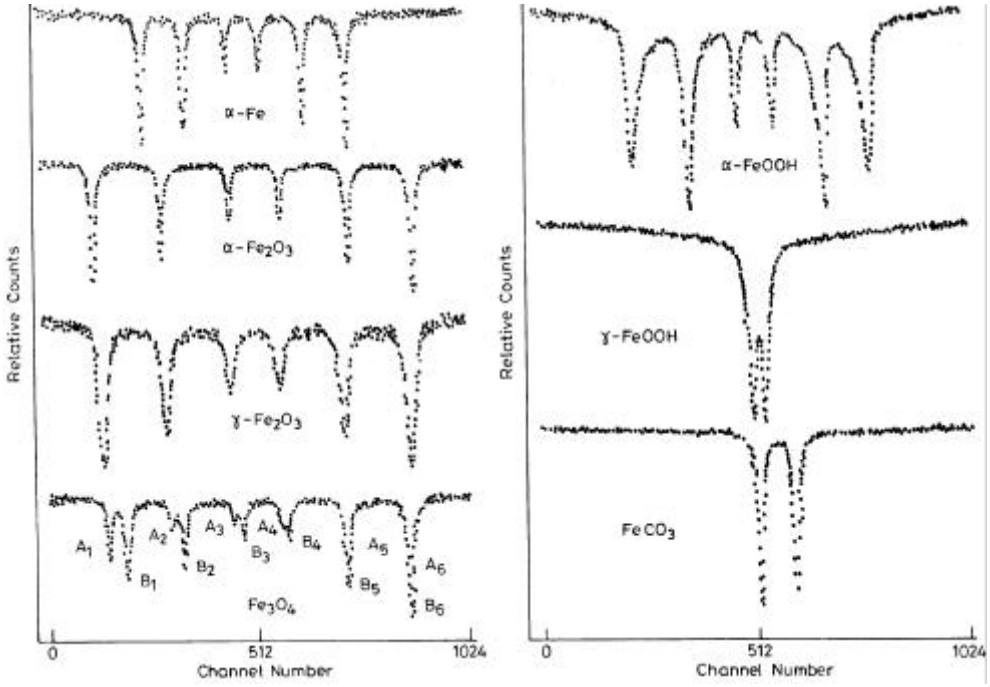

Figure 7. Standard Mössbauer spectra of corrosion products commonly found in rust[67].

appearance of the doublet also indicated that it is due to the very fine particle size of these oxyhydroxides. A sextet should have appeared if these phases were crystalline[56–59]. The asymmetry in the doublet (peak 2) suggested the presence of one more peak with higher quadrupole splitting. This was attributed to the presence of ferrous phosphate[68]. Finally, the sextet provided a magnetic field of 430 kOe, which was lower than that for magnetite. This was explained to result due to the incorporation of some ions in the magnetite lattice[60].

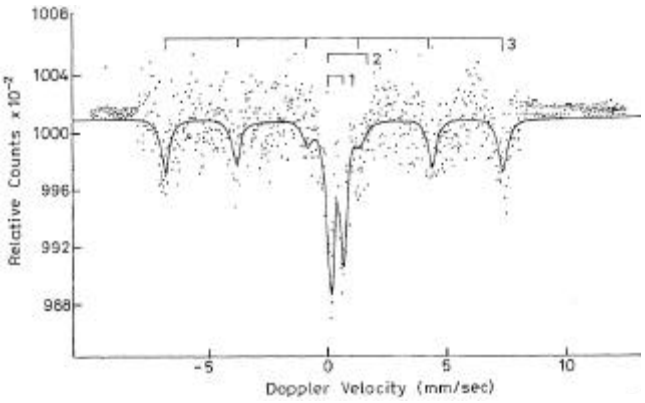

Figure 8. Mössbauer spectrum obtained from the rust of Eran iron[68].

X-ray diffraction

X-ray diffraction (XRD) is one of the most versatile techniques for materials characterization. This was discovered in 1912 by Max von Laue, approximately 18 years after the discovery of X-rays by Wilhelm Roentgen. Shortly thereafter, in England, W. L. Bragg used XRD to determine the crystal structure of halite (NaCl). His father, W. H. Bragg, invented the X-ray spectrometer. The Bragg's established X-ray crystallography. Bragg's law ($2d \sin q = nl$) is the fundamental relationship that describes how the angle of diffraction (q) of an X-ray beam focused on a crystal is related to wavelength (l) and the periodic distance (d) between atomic planes in the crystal. Since periodic atomic distances are unique to individual crystalline compounds, Bragg's law predicts that compounds will have unique diffraction patterns. Consequently, diffraction measurement by XRD is an excellent tool for compound identification when a material has atomic-scale periodicity or crystallinity[69,70]. Computers in modern XRD equipment interactively control goniometer movement, data recording and data reduction. Diffraction patterns can be matched with well-maintained commercial databases[71], and with patterns published in peer-reviewed journals.

The characterization of rust on Deogarh iron utilizing XRD will be provided as an example. The rust layer that was adherent on the iron clamp, was peeled-off from the surface of the sample at one location and diffraction patterns were obtained from both sides of the rust. The diffraction patterns obtained from the inner (i.e. the rust in contact with the metal surface) and outer (i.e. the rust exposed to the atmosphere) regions are shown in Figure 9. The rust in the inner regions was primarily composed of magnetite, while the outer rust contained goethite and lepidocrocite. Interestingly, the presence of phosphate phases

(kryzhanovskite–JCPDF[72] 71–2386, iron hydride phosphate–JCPDF 78–0783 and iron hydrogen phosphate–JCPDF 79–0670) was indicated in the inner rust sample.

Local phase identification is possible in the micro X-ray (μXRD) diffraction technique which uses the same principles as the macro XRD method, but is conducted with a microscopic X-ray beam. The development of X-ray optics in recent years has permitted focusing of an X-ray beam on a small area of several square micrometers[72]. In order to obtain X-ray microbeams with sufficient quantity of photons, brilliant sources must be used and therefore, μXRD experiments are mainly performed on synchrotron beamlines. The synchrotron radiation is an electromagnetic radiation emitted by accelerating charged particles. Synchrotron radiation is quasi continuous and of high brilliance which can be increased to about 10^{19} to 10^{20} photons/s/mm^2/mrad^2 using specific inserting devices as wigglers or undulators. The X-ray optics used for focusing consists of waveguide capillaries, Bragg Fresnel multilayer lenses and Fresnel zone plates[73,74]. A monochromator is used to choose the appropriate wavelength in the hard X-ray domain. The μXRD technique can be utilized to obtain local structural information on scales several hundred μm thick. The high precision of X-ray diffraction patterns permits the identification of complex structures, even with large lattice parameters.

The microdiffraction technique has been successfully employed to understand phase distribution in Eran iron rust[40]. The X-ray μXRD experiments were conducted on the D15 beamline at Laboratoire pour l'Utilisation du Rayonnement Electromagnetique at Orsay, France[74]. A detailed description of the experimental set-up is provided elsewhere[75,76]. One-dimensional diffraction patterns were obtained by circularly integrating diffraction rings using the FIT2D software developed at the European Synchrotron Radiation Facility[77]. The oxide scales formed near the high P containing metallic matrix consisted of a lower amount of crystalline compounds. On the other hand, when the P-content in the matrix was lower, the usual crystalline atmospheric corrosion products (magnetite and goethite) were determined. Finally, in the locations in the oxide where the P content was relatively high, crystalline phosphates were also identified by μXRD[40].

Another advantage with the μXRD technique is that phase distribution profiles can be obtained by analysing a series of μXRD patterns obtained across the rust scales. Such a procedure was adopted for Deogarh iron rust. The outer part was rich in lepidocrocite and goethite, while the inner portion, in magnetite and goethite. The μXRD results were generally in conformity with the XRD results obtained from the rust scale (Figure 9). The microdiffraction patterns obtained from different locations across the rust were analysed to obtain the relative amounts of the phases. Appropriate intensity corrections[78] had to be performed to normalize data. Care was also taken to ensure that the number of diffracted grains was sufficient and randomly distributed. The relative amounts of the various phases in the rust layer in the Deogarh iron rust layer are provided in Figure 10 (Dillmann *et al*., unpublished). The data can be useful in modelling long-term atmospheric corrosion behaviour. The conversion of the initial rust (lepidocrocite) that forms to goethite was indicated by the increasing ratio of goethite with distance into the rust.

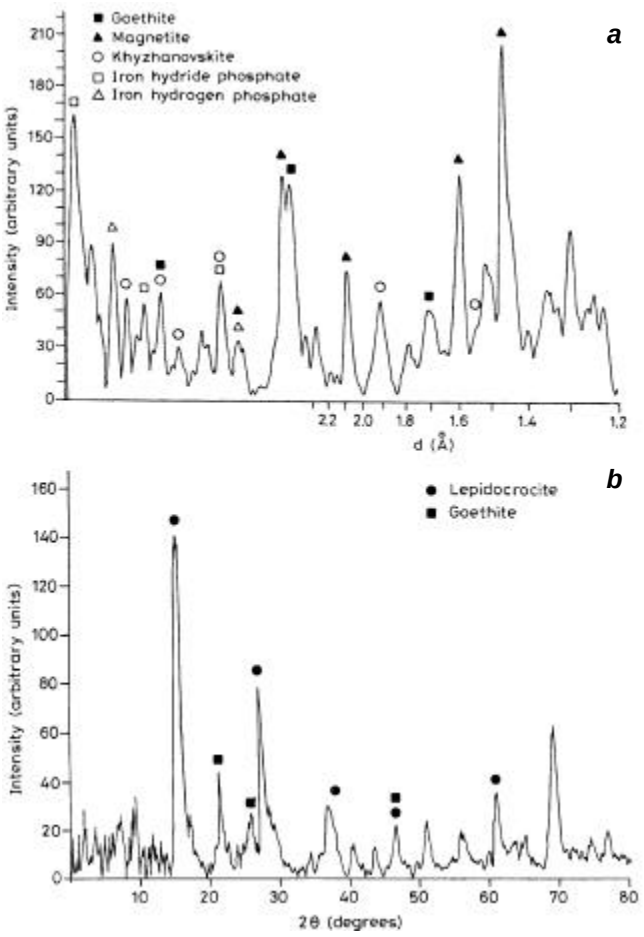

Figure 9. XRD pattern obtained from ***a***, the inner region and ***b***, outer region of rust of Deogarh iron clamp (Dillmann *et al*., unpublished).

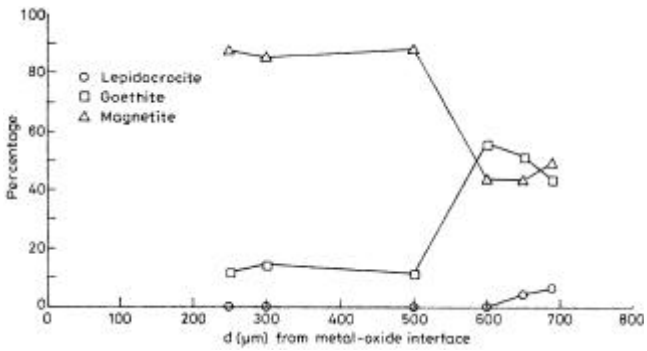

Figure 10. Semi-quantitative profile of various phases determined by analysis of individual μXRD patterns obtained at different locations in the rust of Deogarh iron (Dillmann *et al*., unpublished).

Special care was observed to perform the μXRD experiments at a location where the phases were crystalline. The presence of amorphous phases cannot be understood by X-ray diffraction techniques. This is one of the biggest drawbacks of the XRD technique in general. However, μRAMAN experiments can prove to be useful in these situations.

Conclusion

Techniques for qualitative and quantitative analysis of rust have been reviewed. These have been illustrated using atmospheric rusts on ancient Indian irons. Techniques for microstructural (SEM and optical microscopy) and compositional analyses (EDS, EPMA and μPIXE) have been discussed. The application of important spectroscopic methods (Raman spectroscopy, infrared spectroscopy and Mössbauer spectroscopy) has been illustrated. X-ray diffraction techniques to understand global as well as local character of rust have also been discussed.

1. Neogi, P., *Iron in Ancient India*, Indian Association for Cultivation of Science, Calcutta, 1914.
2. Banerjee, N. R., *Iron Age in India*, Munshiram Mahoharlal, New Delhi, 1965.
3. Mahmud, S. J., *Metal Technology in Medieval India*, Daya Publishing House, New Delhi, 1988.
4. Kuppuram, G. and Kumudamani, K., *History of Science and Technology in Ancient India*, *Metals and Metal Technology*, Sundeep Prakashan, New Delhi, 1989, vol. VI.
5. Chakrabarti, D. K., *Copper and its Alloys in Ancient India*, Motilal Banarasidas, New Delhi, 1996.
6. Biswas, A. K., *Minerals and Metals in Ancient India*, D. K. Printworld, New Delhi, 1996, vols I and II.
7. Anantharaman, T. R., *The Rustless Wonder – A Study of the Delhi Iron Pillar*, Vigyan Prasar, New Delhi, India, 1997.
8. Agrawal, D. P., *Ancient Metal Technology and Archaeology of South Asia: A Pan-Asian Perspective*, Aryan Books International, New Delhi, 2000.
9. Bhardwaj, H. C., *Metallurgy in Indian Archaeology*, Tara Book Agency, Varanasi, 2000.
10. Tripathi, V., *The Age of Iron in South Asia: Legacy and Tradition*, Aryan Books International, New Delhi, 2001.
11. Balasubramaniam, R., *Delhi Iron Pillar – New Insights*, Indian Institute of Advanced Study, Shimla, 2002.
12. Balasubramaniam, R., *Indian J. Hist. Sci*., 2002, **37**, 115–151.
13. Craddock, P. T., Freestone, J. C., Gurjar, L. K., Middleton, A. P. and Willies, L., Zinc in India. In *2000 Years of Zinc and Brass* (ed. Craddock, P. T.), British Museum Occasional Papers No. 50, British Museum, London, 1990.
14. Balasubramaniam, R., Mungole, M. N., Prabhakar, V. N., Sharma, D. V. and Banerjee, D., Studies on ancient Indian OCP period copper. *Indian J. Hist. Sci*., 2002, **37**, 1–15.
15. Balasubramaniam, R. and Mahajan, N., Some metallurgical aspects of Gupta period coin making technology. *Indian J. Hist. Sci*., 2003 (accepted).
16. Graves, H. G., Further, notes on the early use of iron in India. *J. Iron Steel Inst*., 1912, **85**, 187–202.
17. Ghosh, M. K., The Delhi Iron Pillar and its iron. *NML Tech. J*., 1963, **5**, 31–45.
18. Jones, D. A., *Principles and Prevention of Corrosion*, Maxwell Macmillan International Publishing Group, New York, 1992.
19. Uhlig, H. H. and Revie, R. W., *Corrosion and Corrosion Control – An Introduction to Corrosion Science and Engineering*, John Wiley, New York, 1991, 3rd edn.
20. Baboian, R. (ed.), *Electrochemical Techniques for Corrosion*, NACE, Houston, 1977.
21. Annual Book of ASTM Standards, *Wear and Erosion; Metal Corrosion*, ASTM, West Conshohocken, USA, 1999, vol. 02, 03.
22. Lifshin, E., Cahn, R. W., Haasen, P. and Kramer, E. J. (eds), *Characterization of Materials I*, Wiley, New York, 1992, vol. 2A; and *Characterization of Materials II*, Materials Science and Technology, Wiley, New York, 1994, vol. 2B.
23. Evans, U. R. and Taylor, C. A. J, Mechanism of atmospheric rusting. *Corros. Sci*., 1972, **12**, 227–246.
24. Stratmann, M., The atmospheric corrosion of iron. *Ber. Bunsenges. Phys. Chem*., 1990, **94**, 626–639.
25. Misawa, T., Kyuno, T., Suetaka, W. and Shimodaira, S., The mechanism of atmospheric rusting and the effect of Cu and P on the rust formation of low alloy steels. *Corros. Sci*., 1971, **11**, 35–48.
26. Misawa, T., Asami, K., Hashimoto, K. and Shimodaira, S., The mechanism of atmospheric rusting and the protective amorphous rust on low alloy steel. *Corros. Sci*., 1974, **14**, 279–289.
27. Tamura, H., Kawamara, S. and Hagayama, H., Acceleration of the oxidation of Fe^{2+} ions by Fe(III) oxyhydroxides, *Corros. Sci*., 1980, **20**, 963–971.
28. Cook, D. C., Conversion electron and X-ray Mössbauer studies of the corrosion products and surface modifications in stainless steels and weathering steels. *Hyperfine Interact*., 1986, **28**, 891–894.
29. Yamashita, M., Misawa, T., Oh, S. J., Balasubramaniam, R. and Cook, D. C., Mössbauer spectroscopic study of X-ray amorphous substance in the rust layer of weathering steel subjected to long-term exposure in North America. *Corros. Eng*., 2000, **49**, 133–144.
30. Yamashita, M., Miyuki, H., Matsuda, Y., Nagano, H. and Misawa, T., The long-term growth of the protective rust layer formed on weathering steel by atmospheric corrosion during a quarter of a century. *Corros. Sci*., 1994, **36**, 283–299.
31. Suzuki, I., Hisamatsu, Y. and Masuko, N., Nature of atmospheric rust on iron. *J. Electrochem. Soc*., 1980, **127**, 2210–2215.
32. Leygraf, C., Atmospheric corrosion. In *Corrosion Mechanisms in Theory and Practice*, (ed. Marcus, P.), Marcel Dekker, New York, 2002, 2nd edn, pp. 529–562.
33. Miller, F. E., Foss, J. E. and Wolf, D. C., In *Underground Corrosion*, ASTM STP 741, ASTM, West Conshohocken, USA, 1981, pp. 19–45.
34. Goldstein, J. *et al*., *Scanning Electron Microscopy and X-ray Microanalysis*, Kluwer Academic Press, Dordrecht, 2002, 3rd edn.
35. Balasubramaniam, R. and Ramesh Kumar, A. V., Corrosion resistance of the Dhar Iron Pillar. *Corros. Sci*., 2003, **45**, 2451–2465.
36. Balasubramaniam, R., Dhar Iron Pillar. *Bull. Metals Museum*, 2003, **36**, 23–44.
37. Johansson, S. A. E. and Campbell, J. L., *PIXE: A Novel Technique for Elemental Analysis*, John Wiley, New York, 1988.
38. Neff, D. and Dillmann, P., Phosphorus localisation and quantification in archaeological iron artefacts by micro-PIXE analyses. *Nucl. Instrum. Methods Phys. Res. B*, 2001, **181**, 675–680.
39. Dillmann, P. and Balasubramaniam, R., Characterization of ancient Indian iron and entrapped slag inclusions, electron, photon and nuclear microprobes. *Bull. Mater. Sci*., 2001, **24**, 317–322.
40. Dillmann, P., Balasubramaniam, R. and Beranger, G., Characterization of protective rust on ancient Indian iron using microprobe analyses. *Corros. Sci*., 2002, **44**, 2231–2242.
41. Raman, C. V., A new radiation. *Indian J. Phys*., 1928, **2**, 399.
42. Colthup, N. B., Daly, L. H. and Wiberley, S. E., *Introduction to Infrared and Raman Spectroscopy*, Academic Press, New York, 1990, 3rd edn.
43. Skoog, D. A. and Leary, J. J., *Principles of Instrumental Analysis*, Harcourt Brace College Publishers, New York, 1992, 4th edn.

44. Dunn, D. S., Bogart, M. B., Brossiaand, C. S. and Cragnolino, G. A., Corrosion of iron under alternate wet and dry conditions. *Corrosion*, 2000, **56**, 470–488.
45. Nyquist, R. A. and Kagel, R. A. (eds), *IR Spectra of Inorganic Compounds*, Academic Press, New York, 1971.
46. Music, S., Gotic, M. and Popovic, S., X-ray diffraction and Fourier transform infrared analysis of the rust formed by the corrosion of steel in aqueous solutions. *J. Mater. Sci*., 1993, **28**, 5744–5751.
47. Nasrazadani, S., The application of IR spectroscopy to study phosphoric and tannic acid interaction with magnetite, goethite and lepidocrocite. *Corros. Sci*., 1997, **39**, 1845–1860.
48. Raman, A., Kuban, B. and Razvan, K., The application of IR spectroscopy to the study of atmospheric rust systems: I standard spectra and illustrative applications to identify rust phases in natural corrosion. *Corros. Sci*., 1991, **32**, 1295–1306.
49. Balasubramaniam, R. and Ramesh Kumar, A. V., Characterization of Delhi Iron Pillar rust by X-ray diffraction, Fourier infrared spectroscopy and Mössbauer spectroscopy. *Corros. Sci*., 2002, **42**, 2085–2101.
50. Ishii, M. and Nakahira, M., Infrared absorption spectra and cation distributions in $(Mn,Fe)_3O_4$. *Solid State Commun*., 1972, **11**, 209–212.
51. Mössbauer, R. L., Kernresonanzabsorption von Gammastrahlung in Ir^{191}. *Naturwissenschaften*, 1958, **45**, 538.
52. Wertheim, G. K., *Mössbauer Effect: Principles and Applications*, Academic Press, New York, 1964.
53. Leopold, M., *An Introduction to Mössbauer Spectroscopy*, Plenum Press, New York, 1971.
54. Kistner, O. C. and Sanyar, A. W., Evidence for quadrupole interaction of Fe^{57m} and influence of chemical binding on nuclear gamma ray energy. *Phys. Rev. Lett*., 1960, **4**, 412–415.
55. Pound, R. V. and Rebka, G. A., Resonant absorption of the 14.4 KeV *g*-ray from 0.10 μs Fe^{57}. *Phys. Rev. Lett*., 1959, **3**, 554–556.
56. Leidheiser, H. and Music, S., The atmospheric corrosion of iron as studied by Mössbauer spectroscopy. *Corros. Sci*., 1982, **22**, 1089–1096.
57. Stratmann, M. and Hoffmann, K., *In situ* Mössbauer spectroscopic study of reactions within rust layers. *Corros. Sci*., 1989, **29**, 1329–1352.
58. Leidheiser, H. and Czako-Nagy, I., A Mössbauer spectroscopic study of rust formed during simulated atmospheric corrosion. *Corros. Sci*., 1984, **24**, 569–577.
59. Dannon, J., Fe: Metals, alloys and inorganic compound. In *Chemical Applications of Mössbauer Spectroscopy* (eds Goldanaskii, V. I. and Herber, R. H.), Academic Press, New York, 1968, pp. 160–262.
60. Nigam, A. N., Tripathi, R. P. and Dhoot, K., The effect of phosphoric acid on rust studied by Mössbauer spectroscopy. *Corros. Sci*., 1990, **30**, 799–803.
61. Kundig, W., Bommel, H., Constabalis, G. and Lindquist, R. H., Some properties of supported small α-Fe_2O_3 particles determined with the Mössbauer effect. *Phys. Rev*., 1966, **142**, 327–333.
62. Singh, A. K., Ericsson, R., Haggstrom, L. and Gullman, J., Mössbauer and X-ray diffraction phase analysis of rusts from atmospheric test sites with different environments in Sweden. *Corros. Sci*., 1985, **25**, 931–945.
63. Meisel, W., Guttmann, H. J. and Gutlich, P., Influence of phosphoric acid on steel and on its corrosion products: A Mössbauer spectroscopic approach. *Corros. Sci*., 1983, **23**, 1373–1379.
64. Vertes, A. and Czako-Nagy, I., Mössbauer spectroscopy and its application to corrosion studies. *Electrochim. Acta*, 1989, **34**, 721–758.
65. Browen, L. H., De Grave, E. and Vandenborghe, R. E., In *Mössbauer Spectroscopy Applied to Magnetism and Material Science* (eds Long, G. J. and Grandjean, F.), Plenum Press, New York, 1993, vol. 1.
66. Vandenberghe, R. E., Barren, C. A., da Costa, G. M., van San, E. and De Grave, E., Mössbauer characterization of iron oxides and oxyhydroxides: the present state of the art. *Hyperfine Interact*., 2000, **126**, 247–259.
67. Graham, M. J. and Cohen, M., Analysis of iron corrosion products using Mössbauer spectroscopy. *Corrosion*, 1976, **32**, 432–438.
68. Ramesh Kumar, A. V. and Balasubramaniam, R., Corrosion product analysis of ancient corrosion resistant Indian iron. *Corros. Sci*., 1998, **40**, 1169–1178.
69. Cullity, B. D., *Elements of X-ray Diffraction*, Addison-Wesley, New York, 1978, 2nd edn.
70. Suryanarayana, C., *X-ray Diffraction: Practical Approach*, Plenum Press, New York, 1998.
71. JCPDS Powder Diffraction Files, Joint Committee on Powder Diffraction Standards – International Centre for Diffraction Data, Swarthmore, USA, 2001.
72. Bilderback, D. H., Hoffman, S. A. and Thiel, D. J., Nanometer spatial resolution achieved in hard X-ray and laue diffraction experiments. *Science*, 1994, **263**, 201–203.
73. Chevallier, P. and Dhez, P., Hard X-ray microbeam production and application. In *Accelerator-Based Atomic Physics Techniques and Applications*, AIP Press, New York, 1997.
74. Chevallier, P., Dhez, P., Legrand, F., Erko, A., Agafonov, Y., Panchenko, L. A. and. Yakshin, A., The LURE-IMT X-ray fluorescence photon microprobe. *J. Trace Microprobe Tech*., 1996, **14**, 517–539.
75. Dillmann, P., Populus, P., Chevallier, P., Fluzin, P., Béranger, G. and Firsov, A., Microdiffraction coupled with X-ray fluorescence microprobe application in archaeometry. *J. Trace Microprobe Tech*., 1997, **15**, 251–262.
76. Dillmann, P., Regad, B. and Moulin, G., Intermetallic phase identification on Al-Si-Fe hot dip coated steel by X-ray synchrotron microbeam. *J. Mater. Sci. Lett*., 2000, **19**, 907–910.
77. Hammersley, A. P., Svensson, S. O., Thompson, A., Graafsma, H., Kvick, A. and Moy, J. P., Calibration and correction of distortions in two-dimensional detector systems. *Rev. Sci. Instrum*., 1005, **66**, 2729–2733.
78. Nishimura, T., Katayama, H., Noda, K. and Kodama, T., Effect of NaCl–$MgCl_2$ complex on the corrosion behavior of carbon steel in a wet/dry environment. *Corros. Eng*., 2000, **49**, 85–96.

ACKNOWLEDGEMENT. We thank the Archaeological Survey of India for its kind co-operation in studies on ancient Indian iron.

Received 7 April 2003; revised accepted 15 September 2003